THE JOURNAL OF PHYSICAL CHEMISTRY B

pubs.acs.org/JPCB Article

Using Atomic Confining Potentials for Geometry Optimization and Vibrational Frequency Calculations in Quantum-Chemical Models of Enzyme Active Sites

Saswata Dasgupta and John M. Herbert*

Cite This: J. Phys. Chem. B 2020, 124, 1137−1147 Read Online

ACCESS | Metrics & More | Article Recommendations | Supporting Information

ABSTRACT: Quantum-chemical studies of enzymatic reaction mechanisms sometimes use truncated active-site models as simplified alternatives to mixed quantum mechanics molecular mechanics (QM/MM) procedures. Eliminating the MM degrees of freedom reduces the complexity of the sampling problem, but the trade-off is the need to introduce geometric constraints in order to prevent structural collapse of the model system during geometry optimizations that do not contain a full protein backbone. These constraints may impair the efficiency of the optimization, and care must be taken to avoid artifacts such as imaginary vibrational frequencies. We introduce a simple alternative in which terminal atoms of the model system are placed in soft harmonic confining potentials rather than being rigidly constrained. This modification is simple to implement and straightforward to use in vibrational frequency calculations, unlike iterative constraint-satisfaction algorithms, and allows the optimization to proceed without constraint even though the practical result is to fix the anchor atoms in space. The new approach is more efficient for optimizing minima and transition states, as compared to the use of fixed-atom constraints, and also more robust against unwanted imaginary frequencies. We illustrate the method by application to several enzymatic reaction pathways where entropy makes a significant contribution to the relevant reaction barriers. The use of confining potentials correctly describes reaction paths and facilitates calculation of both vibrational zero-point and finite-temperature entropic corrections to barrier heights.

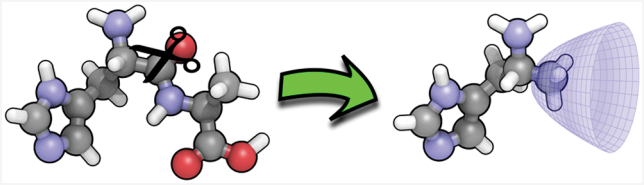

1. INTRODUCTION

Quantum chemistry offers a unique means to understand how enzymatic catalysis works at an atomistic level, providing detailed mechanistic information that is not easily available from experiment. Hybrid quantum mechanics molecular/mechanics (QM/MM) computations combine the accuracy of QM methods for reactive chemistry with the ability of classical MM force fields to provide a good description of conformational energetics, including nonbonded interactions,[1−3] and are widely used in the study of enzymatic catalysis.[4] On the other hand, QM/MM calculations often require specialized software beyond the self-contained quantum chemistry programs that are already in widespread use by many practicing chemists. As such, QM-only ("cluster") models of the active site are a popular, simpler alternative.[5−9] In cases where the quantities of interest are reaction barrier heights and thermodynamics and where large-scale conformational changes of the protein can be ignored, the QM-only approach affords the means to map out a reaction pathway in atomistic detail, identifying the relevant barriers and intermediate species. As compared to a QM/MM molecular dynamics simulation, tracing reaction pathways with QM cluster models may be more satisfying to a mechanistically oriented chemist and may furthermore suggest how chemical synthesis can be used to alter the enzyme's native function. Furthermore, with the continuing improvement of computer hardware and quantum chemistry software, new and more sophisticated *ab initio* methods can be integrated into the active-site model, which may not be feasible for long timescale QM/MM simulations.

In the absence of a full protein backbone, however, steps must be taken to ensure that a truncated model remains faithful to the structure of the enzyme's active site. This usually involves fixing certain atoms in their crystallographic positions (in what has been called the "coordinate locking" approach[5,6,9]), in order to avoid unrealistic deformation of the active-site model during geometry optimization. The model system itself must also be selected carefully. Smaller models may not be faithful to the reaction energetics and may introduce artificial strain (and thereby exaggerate energy differences) in the presence of fixed-atom constraints. Larger models resolve the strain problem, and QM regions with ∼300 atoms have been shown to afford converged energetics.[10−20] In addition to increased cost, however, larger models may be

Received: November 26, 2019
Revised: January 21, 2020
Published: January 27, 2020

https://dx.doi.org/10.1021/acs.jpcb.9b11060
J. Phys. Chem. B 2020, 124, 1137−1147

subject to the "multiple minimum problem" that is well-known in the context of protein folding.[21,22] To avoid this problem, it is necessary to constrain additional atoms close to the truncation points, where the active-site model is trimmed from the crystal structure.[7]

The use of fixed-atom constraints in active-site modeling is simple, popular, and successful, but it is not without problems. The most obvious way to fix certain atoms in space is simply to zero out their contributions to the gradient, but this requires that the optimization be performed using Cartesian coordinates, which is extremely inefficient. Nevertheless, this approach is trivial to implement and is used in several popular quantum chemistry programs including Q-Chem,[23] NWChem,[24] and ADF.[25] Although it is possible to implement fixed-atom constraints using Lagrange multipliers,[26] so that the optimization can be performed more efficiently using internal coordinates, this does not solve the problem of how to handle fixed-atom constraints in vibrational frequency calculations. The usual solution is to give the constrained atoms infinite mass,[27] in which case they do not contribute to the normal modes or to the zero-point energy (ZPE), regardless of whether this is physically correct or not. Calculations on enzymes that use this procedure often report small imaginary frequencies (typically $< 50i$ cm^{-1}) for structures that are interpreted to be local minima,[28−42] which are often brushed aside as numerically unimportant to the magnitude of the ZPE correction. This is certainly true at 0 K, but low-frequency modes make a substantial contribution to the finite-temperature vibrational entropy. Imaginary frequencies of the aforementioned magnitude can alter room-temperature free energies ΔG by 1−5 kcal/mol in some cases,[43,44] and as such the fixed-atom approach renders free-energy calculations unreliable in QM cluster models of enzyme-catalyzed reactions.[32]

That said, vibrational entropy changes in enzymatic reactions are often found to be quite small,[45−50] provided that the reaction does not induce a large-scale conformation change in the protein, so entropic effects are frequently ignored in the QM-only approach. This is justified by the observation that many enzymatic reactions proceed via an induced-fit or "lock and key" mechanism, for which it may be reasonable to assume that the vibrational entropy is approximately constant along the reaction path and therefore ΔH alone dictates the fate of the reaction.[9] Even so, reliance on enthalpy alone is problematic for reactions that liberate or consume a gaseous species such as CO_2. In such cases, the entropic effect is significant and cannot be neglected, since the number of atoms in the active site is not conserved.[37,40,41,51,52]

In the present work, we show that the introduction of soft harmonic confining potentials for the "anchor atoms" accomplishes the same goal as fixing those atoms in space but without the problems outlined above. In a sense, these confining potentials are a form of penalty-function optimization,[26] albeit a physically motivated one. This approach fits naturally within a standard vibrational frequency calculation or reaction-path optimization algorithm, with only trivial modifications to the software. Operationally, this facilitates the use of what are effectively fixed-atom constraints, but unlike traditional fixed-atom constraints the use of harmonic confining potentials does not increase the complexity of the quantum chemistry calculations.

2. METHODS

In the present work, we introduce an additional, classical term into the energy expression, namely,

$$V_{\text{conf}}(\mathbf{r}_1, \mathbf{r}_2, \ldots) = \frac{1}{2}\sum_i k \, \|\mathbf{r}_i - \mathbf{r}_i^0\|^2 \tag{1}$$

This potential confines the ith atom (with coordinates $\mathbf{r}_i$) to its crystallographic position, $\mathbf{r}_i^0$. In the present work, active-site models are trimmed from the protein at the C_α carbon of a peptide bond, so the force constant k is chosen to resemble that of a C−C bond. The first derivative of V_{conf} is added to the gradient of the electronic energy and then the geometry optimization is performed without constraints, using delocalized (non-redundant) internal coordinates.[53] Vibrational frequency calculations can be performed without modifying the atomic masses, by adding the second derivative of V_{conf} to the Hessian of the electronic energy. This method has been implemented in a locally modified version of Q-Chem[23] and verified against finite-difference calculations (Table S1).

Figure 1 provides a pictorial illustration. The confining potential V_{conf} replaces a bond between the active-site model

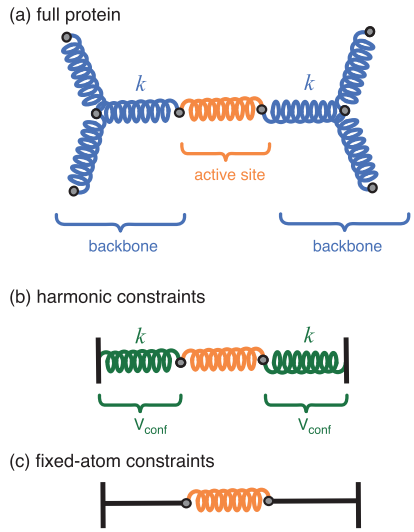

Figure 1. Cartoon illustration of a flexible active site tethered to either (a) a fully flexible protein backbone, (b) a fictitious set of springs that confine the C_α atoms in space, or else (c) rigid fixed-atom constraints applied to the C_α atoms.

and the protein backbone with a spring having a similar force constant (Figure 1b). The harmonic motion of the confined atoms affords the flexibility necessary to obtain correct energy profiles and ZPE corrections, whereas the fixed-atom method locks down the terminal atom in space (Figure 1c).

In the applications presented below, active-site models are constructed by clipping at the C_α carbon and replacing this carbon atom with a methyl group, with only the C_α atom (not the methyl hydrogen atoms) subjected to the confining potential in eq 1. To test this method and to determine an appropriate force constant k in eq 1, we examine the spectrum of vibrational frequencies obtained for the dipeptide Gly−Ala, with methyl capping atoms subject to confining potentials. Figure 2 plots the difference $\Delta\nu$ between vibrational frequencies computed for this confined model versus those computed for the free dipeptide without any constraints, for several different values of k. Stiffer force constants afford larger

https://dx.doi.org/10.1021/acs.jpcb.9b11060
J. Phys. Chem. B 2020, 124, 1137−1147

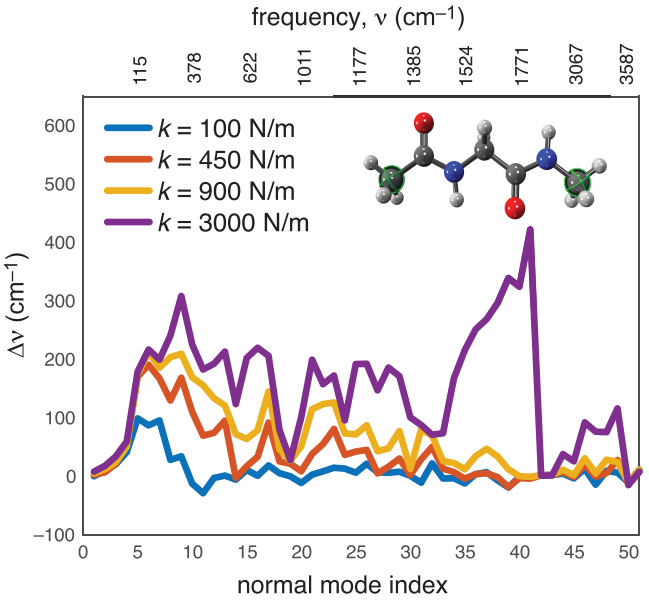

Figure 2. Differences $\Delta\nu$ in vibrational frequencies of Gly−Ala, comparing the free dipeptide to one in which both terminal carbon atoms are subject to harmonic confinement using various values of the force constant k in eq 1. All calculations were performed at the B3LYP/6-31G* level of theory. As in subsequent enzyme calculations, the anchor C_α atoms (indicated in green in the ball-and-stick model) are replaced by methyl groups. The free and confined dipeptide structures were each optimized separately.

deviations (shifted to higher frequencies) as compared to frequencies computed for the constrained structure, and we settled on a value of k = 450 N/m. This is similar to the force constant for a C−C single bond.[54] For this and similar values of k, errors appear primarily in the modes below 1000 cm^{-1}.

3. DECARBOXYLATION OF α-SUBSTITUTED ARYL MALONATES BY AMDASE

3.1. Background. Arylmalonate decarboxylase (AMDase) catalyzes the decarboxylation of α-aryl-α-methyl malonates to afford enantiomerically pure α-aryl propionates,[55−57] which are useful precursors in the synthesis of anti-inflammatory drugs.[58,59] The two-step mechanism (Scheme 1) proceeds via formation of an enediolate intermediate.[60] The intermediate is selectively protonated at the *si* face by Cys188 of AMDase, resulting in the *R* isomer of the aryl propionate product. Various malonic acid substrates can be processed by AMDase,[55−57,61] although the scope is limited to those having an alkyl or aryl group in the α position. One substituent of the disubstituted malonic acid should be an electron-withdrawing group (Ar− in Scheme 1), as this helps to stabilize the negative charge in the enediolate intermediate, while the other substituent should be no bulkier than methyl because a steric effect destabilizes the rate-determining step.[56,57] In the presence of a bulky electron-withdrawing group, AMDase reacts with the substrate in an enantioselective fashion to afford the pure *R* isomer,[60] but when the substrate is smaller (e.g., methyl vinyl malonate), the reaction affords a racemic mixture of products, as the *R* and *S* reaction barriers are comparable in the absence of steric hindrance.[56,57]

Scheme 1. Mechanism for the Decarboxylation of Malonate by AMDase, Resulting in an α-Aryl Propionate of the Form $ArRHCOO^-$

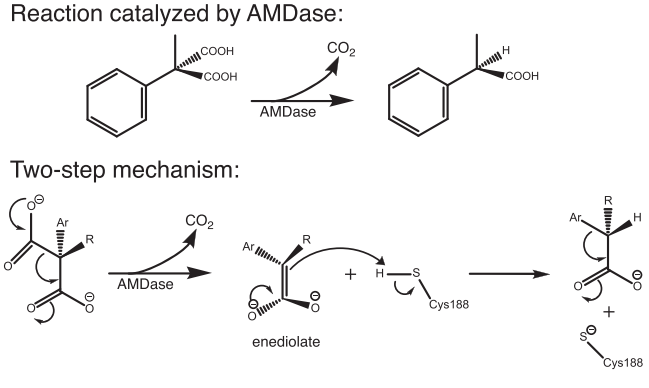

From the crystal structure (PDB: 3IP8),[61] it has been determined that the presence of a dioxyanion hole in the active site is key to stabilization of the enediolate complex, as this hole can bind with the carboxylate of substrate via six hydrogen bonds;[61,62] see Figure 3. Along with the oxyanion holes, there are two cavities present in the active site: a larger one that is solvent exposed and a smaller one that is hydrophobic.[62,61] The bulky substituent (phenyl group in Figure 3) resides on the solvent-exposed hole, leaving the enantiotopic carboxylate group in the hydrophobic pocket. Dioxyanion holes help to stabilize the *pro-S* carboxylate group via hydrogen bonding, culminating in protonation of the enediolate intermediate from the *si* face, resulting in formation of the *R* product. The presence of Cys188 is also important in obtaining the desired stereochemistry of the product, and replacing this residue in the wild-type enzyme results in different stereoselectivity or reduction in the rate.[63−65] Isotopic labeling experiments with ^{13}C and ^{18}O reveal formation of the *R* product with stereochemical inversion at the α-carbon. It is also demonstrated that elimination of the *pro-R* carboxylate group is the key for decarboxylation, which appears to be the rate-limiting step, since no isotope effect is observed in deuterated water.[66]

Quantum-chemical studies of active-site models bolster the case for the two-step mechanism in Scheme 1, consisting of decarboxylation of the substrate followed by protonation of the enediolate complex.[37] A small model with 81 atoms that includes the dioxyanion hole and the Cys188 residue affords energetics that are consistent with this mechanism but is unable to emulate the enantioselectivity that is observed experimentally.[37] To describe the enantioselectivity, a larger model consisting of 223 atoms with additional active site residues around the dioxyanion hole was considered.[37] Calculations using a substrate with a bulky substituent [methyl(phenyl)malonate, Figure 3] suggest that binding of the substrate to the enzyme is key to enantioselectivity, as there are substantial differences between the binding affinities of the substrate leading to the *R* product versus the *S* product. In contrast, the energetic difference between these binding motifs is quite small in the case of methyl(vinyl)malonate, due to the lack of a steric effect in the absence of the bulky phenyl group.[37]

In these cluster model calculations, the traditional "coordinate-lock" formalism has been used,[37] or in other words what we have called the fixed-atom approach. A disadvantage of that approach in the context of AMDase is that it makes the whole model system too rigid, which artificially amplifies the steric effect.[37]

https://dx.doi.org/10.1021/acs.jpcb.9b11060
J. Phys. Chem. B 2020, 124, 1137−1147

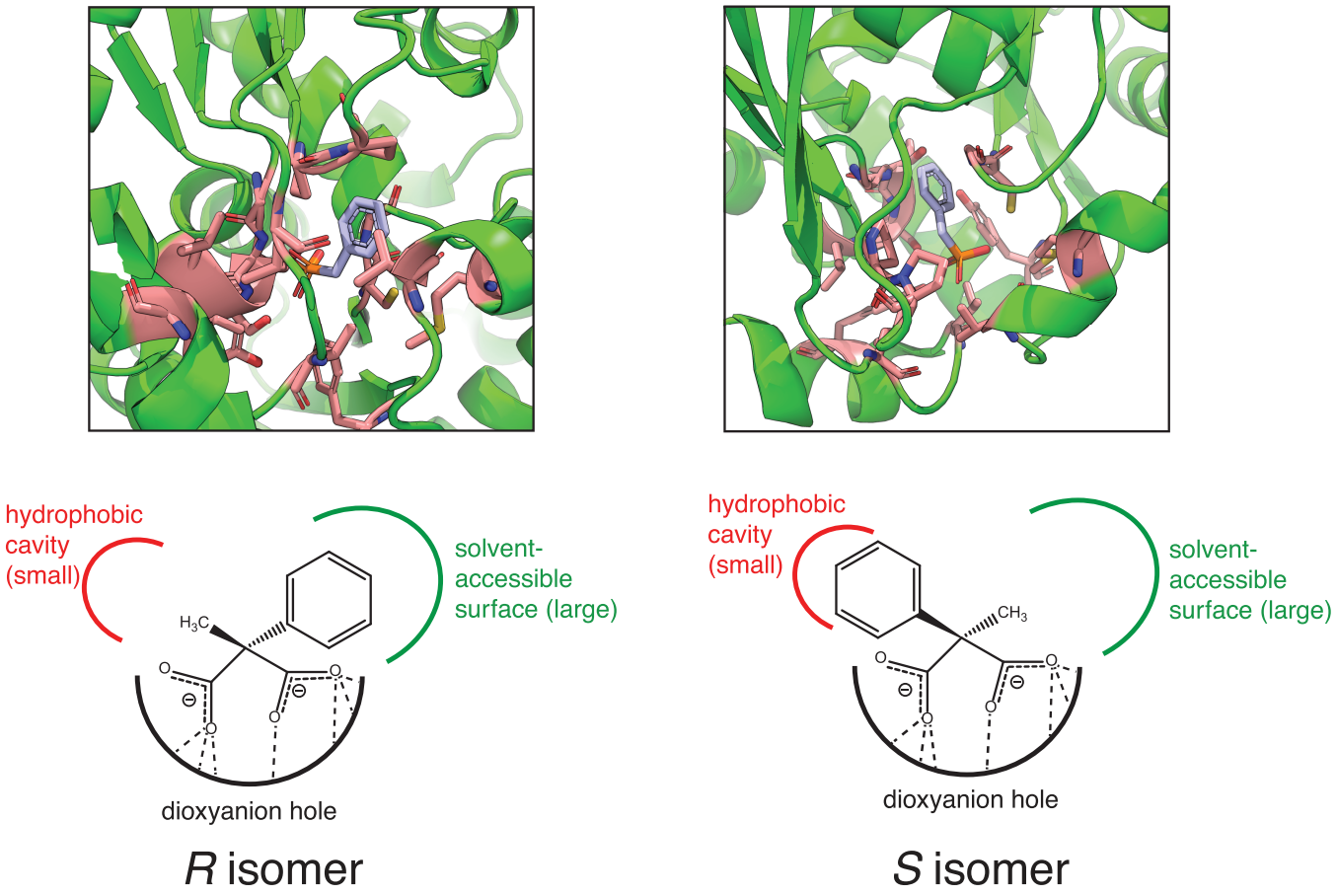

Figure 3. Schematic depictions (based on ref 37) of the *R* and *S* enantiomers of the intermediate enediolate in the active site of AMDase. Note the steric clash of the phenyl group in the hydrophobic pocket, in the case of the *S* isomer.

Furthermore, the fact that the AMDase-catalyzed decarboxylation reaction liberates CO_2 suggests that changes in vibrational entropy cannot be neglected in the first step of Scheme 1. In such cases, fixed-atom optimization is not a good choice, as the use of rigid constraints makes the ZPE correction ambiguous, and may result in imaginary frequencies corresponding to bending modes associated with the fixed atoms.

In what follows, we will compute the reaction profile for the two-step mechanism in Scheme 1 using both fixed-atom constraints and harmonic confining potentials.

3.2. Model I. We will consider the decarboxylation of methyl(phenyl)malonate by AMDase, using two different active-site models from ref 37. The first of these is the 81-atom model shown in Figure 4, which consists of the residues needed to form the dioxyanion hole. These include Gly74, Thr75, Ser76, Tyr126, and Gly189 along with the proton source Cys188. This model lacks the solvent-exposed and hydrophobic cavities.[37] All amino acids were truncated at C_α except for tyrosine, which was replaced by phenol (following ref 37), and the model system has a net charge of −2. The positions of five anchor atoms are constrained; these atoms are indicated in Figure 4.

All calculations for model I have been performed using the B3LYP functional with the D3(BJ) dispersion correction.[67,68] Geometry optimizations and harmonic frequency calculations were performed using the 6-31G(d,p) basis set, with additional single-point energies (at optimized geometries) computed using the 6-311+G(2d,2p) basis set. The SG-1 quadrature

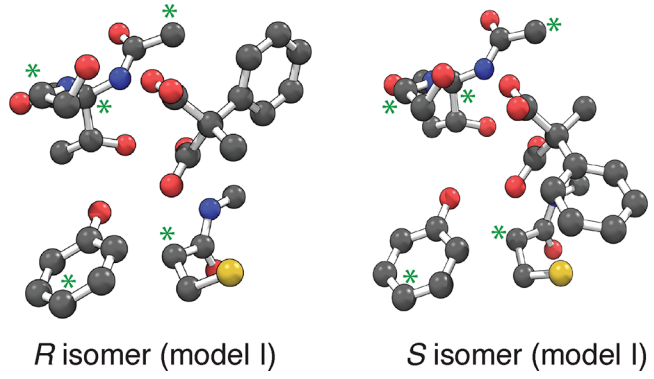

Figure 4. Optimized structures of the *R* and *S* isomers of the enzyme/substrate complex of methyl(phenyl)malonate and AMDase, corresponding to the 81-atom active-site model I of ref 37. Hydrogen atoms are omitted for clarity, and arrows indicate the anchor asterisks.

grid[69] is used for all DFT calculations. Solvation effects have been incorporated using the conductor-like polarizable continuum model (C-PCM),[70] in its intrinsically smooth formulation,[71,72] with $\varepsilon = 4$ and a van der Waals cavity for the solute, constructed from atomic radii $r_{atomic} = 1.2r_{vdW}$. The energetics reported below correspond to the B3LYP+D3(BJ)/6-311+G(2d,2p) in C-PCM, with vibrational ZPE corrections.

Optimized structures for the *R* and *S* isomers of the enzyme/substrate complex are shown in Figure 4, where the stereochemical designation represents that of the final product. Either fixed-atom or else harmonic constraints were applied to

https://dx.doi.org/10.1021/acs.jpcb.9b11060
J. Phys. Chem. B 2020, 124, 1137−1147

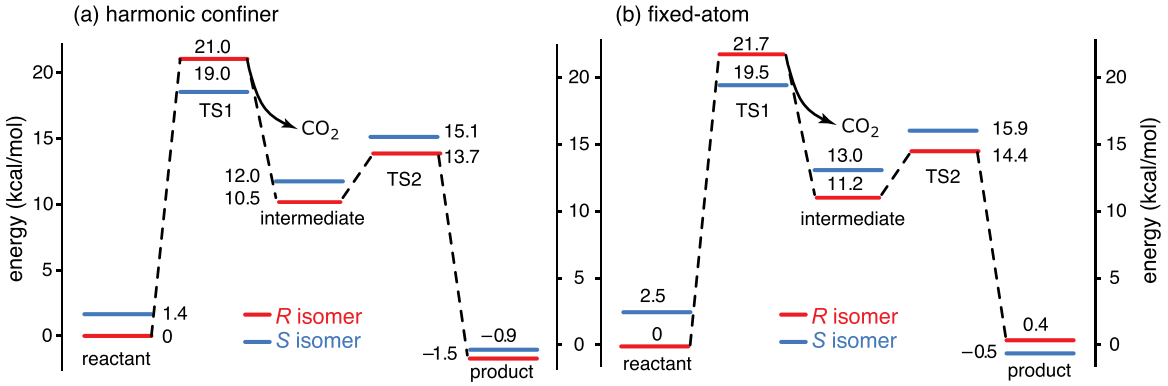

Figure 5. ZPE-corrected energy profiles for model I (Figure 4) of the decarboxylation of methyl(phenyl)malonate by AMDase, using (a) harmonic confining potentials versus (b) fixed-atom constraints. Energies are reported at the B3LYP+D3(BJ)/6-311+G(2d,2p)//B3LYP+D3(BJ)/6-31G(d,p) level, in continuum solvent with ε = 4. Transition states and intermediates correspond to the two-step mechanism in Scheme 1. Optimized structures of the reactant species are shown in Figure 4.

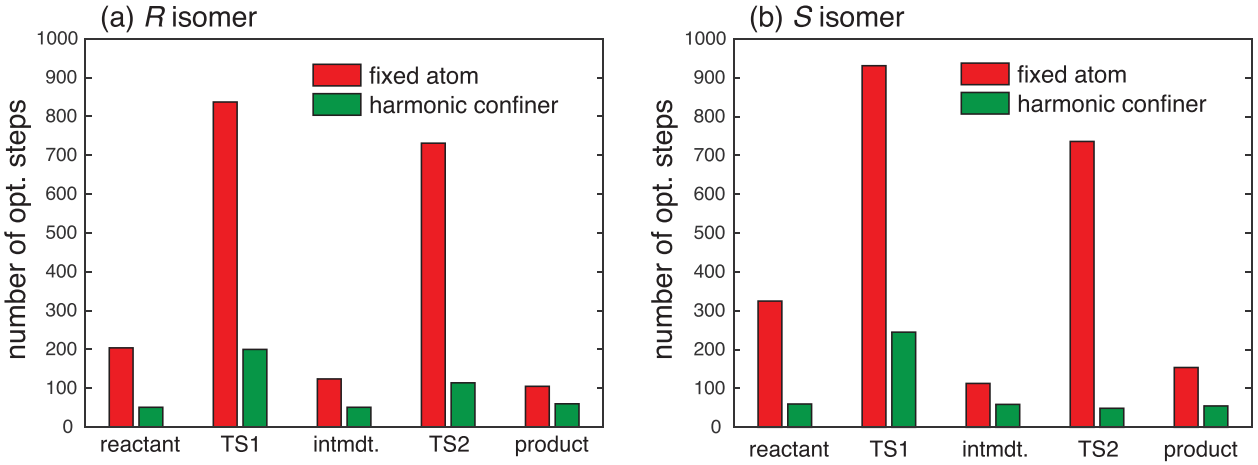

Figure 6. Number of optimization steps required to locate various stationary points for (a) the *R* isomer and (b) the *S* isomer for model I (Figure 4) of the decarboxylation of methyl(phenyl)malonate by AMDase. Stationary points correspond to the reaction profiles depicted in Figure 5. Cartesian coordinates are used for the fixed-atom optimizations, whereas delocalized internal coordinates are used for optimizations with harmonic constraints.

the same five atoms that are indicated in Figure 4, and both approaches afford similar structures for each stationary point. (See Figure S1 for an overlay of structures optimized using either set of constraints, and note in particular that the optimized positions of the anchor atoms deviate from their crystallographic positions $\mathbf{r}_i^0$ by no more than 0.04 Å, as shown in Figure S2.) As such, a one-to-one comparison of the reaction energy profiles is appropriate. The energy difference between the *R* and *S* isomers of the reactants is ≈1.1 kcal/mol larger with fixed-atom constraints as compared to harmonic constraints; see Figure 5.

In the two-step mechanism of Scheme 1, the intermediate species is stabilized by six hydrogen bonds to the dioxyanion hole and the entropic effect is significant when proceeding from the first transition state (TS1 in Figure 5) to the intermediate, partly due to the translational entropy of CO_2: S_{trans} × (298 K) = 11.1 kcal/mol. The fixed-atom method affords several small imaginary frequencies for the stationary points, whereas all of the frequencies are real when harmonic constraints are used. As compared to the harmonic-confiner approach, the fixed-atom method affords energies that are slightly higher (by up to 1 kcal/mol) for both the *R* and *S* isomers of TS1 and the intermediate species. The proton-transfer barrier (intermediate → TS2) is about the same in both cases. The initial barrier (reactants → TS1), which constitutes the rate-determining step, is somewhat exaggerated in all of these calculations as compared to the experimental estimate of 14−16 kcal/mol.[57,73] The harmonic-confiner approach predicts that the *R* isomer of the products is more stable as compared to the *S* isomer, in agreement with a previous theoretical study using the B3LYP-D2 functional;[37] however, the fixed-atom approach affords *S* as the lower-energy isomer. Overall, these calculations support the established mechanism regardless of which approach is used to constrain the anchor atoms, albeit with slightly different energetics depending on the nature of the constraints.

Along with adding flexibility to the model system that eliminates imaginary frequencies and thereby affords proper local minima, use of harmonic constraints significantly accelerates structure optimizations by allowing them to proceed in internal coordinates. (As mentioned in the Introduction, several popular quantum chemistry packages require optimizations using fixed atoms to use Cartesian coordinates.) Figure 6 compares the number of optimization steps that are required to locate the various stationary points for model I of methyl(phenyl)malonate in the active site of

https://dx.doi.org/10.1021/acs.jpcb.9b11060
J. Phys. Chem. B 2020, 124, 1137−1147

AMDase, comparing fixed-atom optimization in Cartesian coordinates to harmonically confined optimization in delocalized internal coordinates. The former often takes many hundreds of steps, a number that is dramatically reduced by the method introduced here, without the need to modify the electronic structure program beyond the trivial addition of eq 1 and its gradients. Furthermore, even if a Lagrange multiplier algorithm is employed,[26] in order to use internal coordinates in conjunction with fixed-atom optimization, there remains an issue with vibrational frequency calculations, which are subject to artifacts due to the need to set the anchor-atom masses to infinity. In our experience, setting these masses to infinity results in imaginary frequencies more often than not. This problem has been noted in other studies as well.[28−42]

3.3. Model II. A second, larger model of the AMDase active site that includes the hydrophobic and solvent-exposed cavities was introduced in ref 37. In addition to the amino acid residues included in model I, this model includes additional residues Pro14, Pro15, Leu40, Val43, Tyr48, Val156, Met159, Gly190, and Leu77, the last of which is hydrogen-bonded to Ser76. In all, the model contains 223 atoms with 17 anchor atoms and a net charge of −2. Geometry optimizations and single-point energies were computed at the same levels of theory as for model I, and optimized enzyme/substrate complexes corresponding to the *R* and *S* product isomers are shown in Figure 7. (Not all of the anchor atoms are visible in the figure; see Table S2 for the complete list. Figure S3 shows the optimized anchor atoms deviate from their initial crystallographic positions by no more than 0.035 Å.)

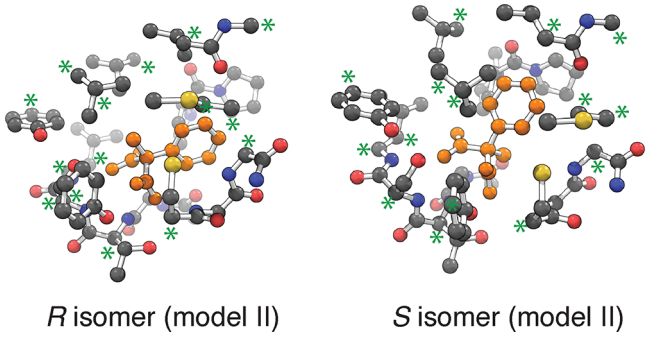

Figure 7. Optimized structures of the *R* and *S* product isomers corresponding to the 223-atom "model II" (as proposed in ref 37) of methyl(phenyl)malonate (shown in orange) in the active site of AMDase. Hydrogen atoms are omitted for clarity, and asterisks indicate the anchor atoms. There are a total of 17 anchor atoms, not all of which are visible here.

In the case of the enzyme/substrate complex leading to the *R* isomer, the bulky phenyl group stays in the large solvent accessible cavity; see Figure 3. For the *S* isomer, the hydrogen bonds of the carboxylate moieties and the dioxyanion hole are intact but the methyl group inhabits the solvent-accessible cavity, leaving the phenyl group exposed to the smaller, hydrophobic cavity. As such, the *S* complex is destabilized relative to *R*, by 6.4 kcal/mol in the case of harmonic constraints but 12.4 kcal/mol when optimized with fixed-atom constraints. (These relative energies are listed on the reaction profile for model II that is presented in Figure 8.) The rigidity of the model when fixed-atom constraints are employed has the effect of exaggerating the energy gap, leaving the atoms involved in the reaction caged inside a fixed framework that is unable to expand even by a fraction of a C−C bond length.

Examination of the energy profile for the *R* isomer (Figure 8) reveals it to be quite similar to that of model I except that the rate-limiting TS1 barrier height is significantly reduced, from 19.0 kcal/mol (model I) to 14.8 kcal/mol (model II). The latter is in much better agreement with the experimental estimate of 14−16 kcal/mol.[37,73] The change in the TS1 barrier height is smaller for the *S* isomer: 21.0 kcal/mol (model I) versus 22.3 kcal/mol (model II). The difference is that the enediolate intermediate is destabilized by the steric hindrance, with a large phenyl substituent that stays in the small solvent-accessible cavity. To avoid this, the substrate stays farther away from the active site and is therefore less accessible. This difference becomes more apparent for TS2, as inversion of the stereochemistry causes additional steric repulsion with the large substituent, in the case of the *S* isomer, resulting in a much larger TS2 barrier as compared to that predicted by model I.

Overall, both models support the feasibility of the two-step mechanism in Scheme 1, but only the larger model explains the enantioselectivity. We should emphasize that these were the conclusions reached in the original computational study of ref 37, in which models I and II were introduced and optimized using fixed-atom constraints. In the case of model II, however, the present work demonstrates that the more rigid fixed-atom approach predicts a much larger difference between the energies of the *R* and *S* enzyme/substrate complexes and a much larger barrier height for TS2. In addition to demonstrating that harmonic constraints relieve the artificial strain of the fixed-atom models, the main result of the present study is the demonstration that the number of optimization cycles can be dramatically reduced, without the need for specialized optimization algorithms, via the use of simple harmonic confining potentials.

4. TAUTOMERIZATION OF α-KETO ACIDS BY 4-OXALOCROTONATE TAUTOMERASE

The bacterial enzyme 4-oxalocrotonate tautomerase (4-OT) catalyzes tautomerization of unsaturated α-keto acids, as shown in Scheme 2. Its crystal structure reveals a trimer of dimers (Figure 9a),[74] with each monomer composed of 62 amino acids and six active sites present at the dimer interface.[75,76] The general mechanism of the reaction catalyzed by 4-OT is presented in Scheme 3 and is supported by both theoretical calculations[28,77−79] and experimental studies.[80−82] In this mechanism, a proline residue (Pro1) snatches a proton from the C3 position of the α-keto acid, whence the latter undergoes a structural change due to conjugation, giving rise to a different tautomer by releasing the C5 proton to proline. The proline remains in the deprotonated state, which helps it to act as a Lewis base for the reaction.

Three Arg residues of the trimer play an important role to stabilize the carboxyl and carbonyl groups of the substrate by forming hydrogen bonds.[28,75−77,83−86] QM/MM studies have shown that barrier heights are larger when these residues are not included in the QM region.[77,86] Only a moderate lowering of the barriers is observed when single-point calculations are performed on QM regions enlarged to include these three residues, but upon subsequent geometry optimization using the larger QM region, the resulting structures exhibit much lower barrier heights and a different binding motif for Arg39″, as compared to models based on QM regions that exclude the

https://dx.doi.org/10.1021/acs.jpcb.9b11060
J. Phys. Chem. B 2020, 124, 1137−1147

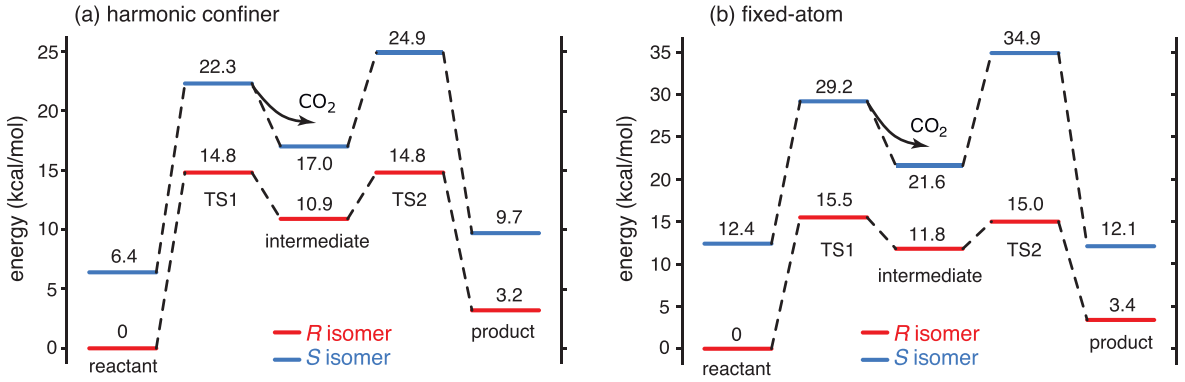

Figure 8. ZPE-corrected energy profiles for model II (Figure 7) of the decarboxylation of methyl(phenyl)malonate by AMDase, using (a) harmonic confining potentials versus (b) fixed-atom constraints. (Note that the energy scale is different in the two panels.) Energies are reported at the B3LYP+D3(BJ)/6-311+G(2d,2p)//B3LYP+D3(BJ)/6-31G(d,p) level, in continuum solvent with $\varepsilon = 4$. Transition states and intermediates correspond to the two-step mechanism in Scheme 1. Optimized structures of the reactant species are shown in Figure 7.

Scheme 2. Tautomerization of α-Keto Acids Catalyzed by the Enzyme 4-OT

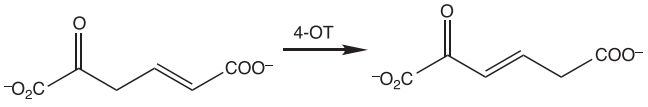

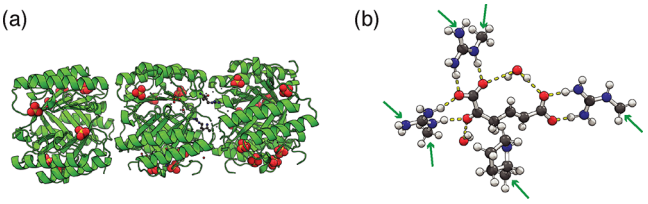

Figure 9. Model of 4-OT for the QM calculations: (a) as a part of the full enzyme and (b) separated from the rest of the protein backbone. In part b, the anchor atoms are indicated by arrows and deviate by no more than 0.02 Å from their initial crystallographic positions (see Figure S4).

Scheme 3. Proposed Mechanism of α-Keto Acid Tautomerization Catalyzed by 4-OT. Adapted from ref 28. Copyright 2007 Elsevier.

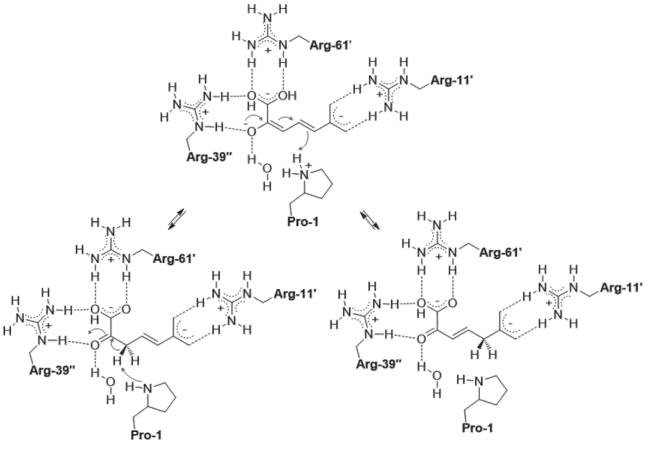

three Arg residues.[86] QM cluster studies support the mechanism in Scheme 3 and suggest that the ability of Pro1 to act as a base helps the substrate to tautomerize.[28] The calculations suggest that proton transfer from C3 to Pro1 is the rate-determining step. These calculations predict a very stable intermediate species, consistent with the fact that the pK_a of Pro1 in the active site is similar to that of the substrate.

The 4-OT mechanism is an important test case for QM cluster models because charge separation in the intermediate makes this mechanism difficult to model accurately if the QM region is small. In ref 28, a smaller model system with 77 atoms (Figure 9b) was benchmarked against a larger model containing 177 atoms, and both were found to support the two-step mechanism outlined in Scheme 3. The role of the continuum dielectric constant proves to be interesting in this case. For the larger model, the value of ε has almost no effect over the range $\varepsilon = 2-80$.[28] This indicates that the residues explicitly included in the QM region provide the necessary polarization effects. In contrast, the value of ε does affect the energetics in the case of the smaller QM model, although the effect is small and saturates quickly, i.e., there is little difference between results obtained using $\varepsilon = 4$ and those with $\varepsilon = 16$.[28]

To compare the energetics of the fixed-atom versus the harmonic-confiner methods, we have calculated the energetics for the smaller "model system A" of ref 28, which qualitatively reproduces the results inferred from the larger model system. This model is made up of the substrate 2-oxo-4-hexenedioate, the proline residue Pro1 that serves as the proton sink, the three aforementioned arginine resides (Arg39″, Arg61′, Arg11′), and finally two crystallographic water molecules (W1 and W2). The model contains 77 atoms and has an overall charge of +1. As for the AMDase example in section 3, optimizations and frequency calculations were performed at the B3LYP-D3(BJ)/6-31G(d,p) level followed by single-point energy calculations at the B3LYP-D3(BJ)/6-311+G(2d,2p) level. The C-PCM dielectric continuum model was included using either $\varepsilon = 4$, 8, or 16. Six different anchor atoms were confined, as indicated in Figure 9b. Energy profiles are depicted in Figure 10.

Both methods of constraining the anchor atoms support the mechanism presented in Scheme 3, in which Pro1 acts as a base to shuttle a proton from the C3 to the C5 position of the substrate. For this small model system, both TS1 and the intermediate species exhibit some stabilization due to the dielectric continuum, which is unsurprising given that the first step of the mechanism is proton transfer resulting in a positive charge on Pro1 and a negative charge on substrate. Unlike a previous QM cluster study of this mechanism,[28] however, our results exhibit two distinct transition states regardless of the value of ε, including the vacuum case ($\varepsilon = 1$). In the

https://dx.doi.org/10.1021/acs.jpcb.9b11060
J. Phys. Chem. B 2020, 124, 1137−1147

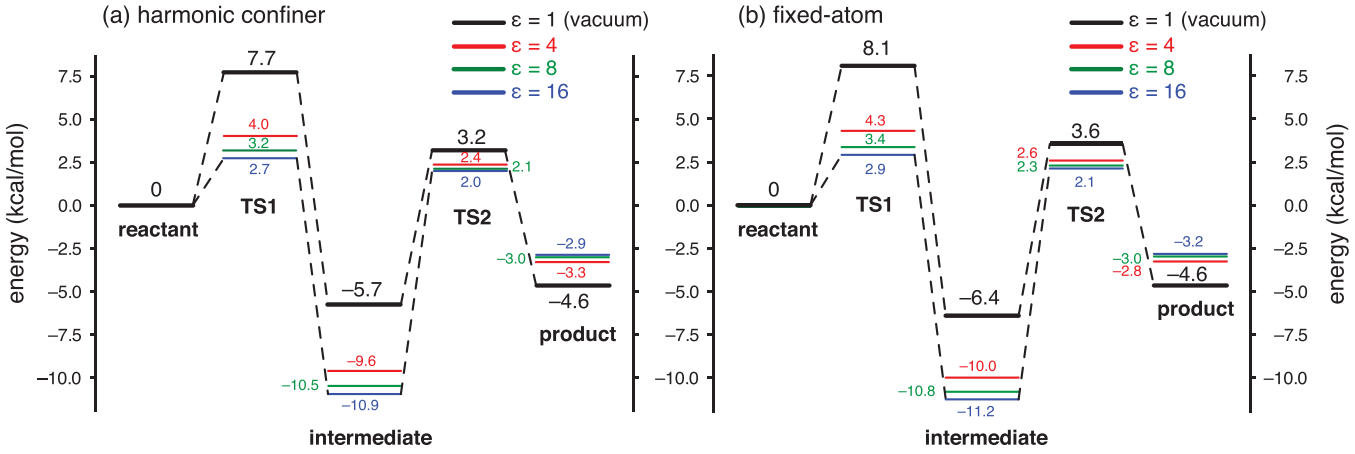

Figure 10. ZPE-corrected energy profile for tautomerization of 2-oxo-4-hexenedioate catalyzed by 4-OT using (a) soft harmonic constraints or (b) fixed-atom constraints. Calculations are performed at the B3LYP+D3(BJ)/6-311+G(2d,2p)//B3LYP+D3(BJ)/6-31G(d,p) level of theory, in a continuum solvent with various dielectric constants.

calculations reported in ref 28, which were carried out at an identical level of theory [B3LYP/6-31G(d,p)] except for the absence of a dispersion correction, only a single transition state is obtained when $\varepsilon = 1$. Two distinct transition states, corresponding to the mechanism in Scheme 3, begin to emerge when $\varepsilon = 2$, and for $\varepsilon \geq 4$, there is an intermediate that is clearly lower in energy than TS2.[28]

In the present study, the intermediate emerges as a much more stable species that is present even for $\varepsilon = 1$, and the energetics that we obtain for this small model system ("model A" of ref 28) are in better agreement with the larger model system ("model B") as compared to calculations on the smaller model system in the original work of ref 28. That the Arg39″ residue and the water molecule W1 are sufficient to stabilize the negative charge that develops on the substrate in the transition states and in the intermediate is supported by both of the QM cluster models. Our results also confirm that the presence of a dielectric continuum ($\varepsilon > 1$) does make a difference in the energy profile that is obtained but that the effect is largely saturated by $\varepsilon = 4$.

Figure 11 shows the cost comparison between the two methods for imposing constraints on the anchor atoms. As in the AMDase example of section 3, the number of optimization cycles is dramatically reduced when the fixed-atom constraints are replaced by soft confining potentials, as this enables the optimization to proceed via delocalized internal coordinates. The fixed-atom approach results in small imaginary frequencies, whereas each of the local minima exhibits only real frequencies when harmonic confining potentials are used.

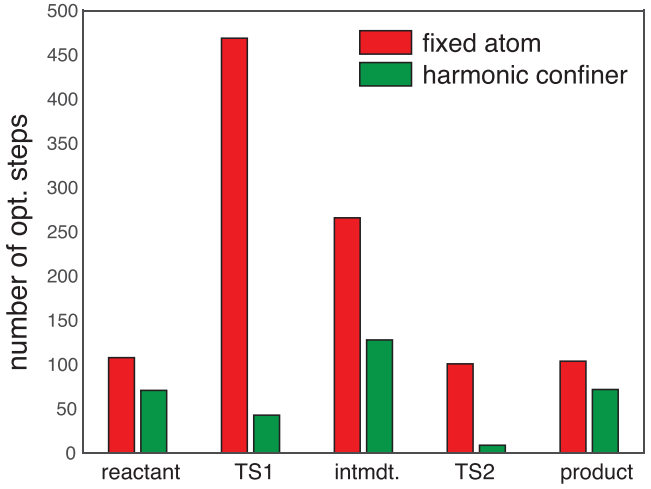

Figure 11. Number of optimization steps required to locate the stationary points in Figure 10 for the tautomerization of 2-oxo-4-hexenedioate catalyzed by 4-OT. The fixed-atom optimizations were performed using Cartesian coordinates, whereas delocalized internal coordinates were used with harmonic confining potentials.

5. CONCLUSIONS

Examples for three structural models of two different enzyme-catalyzed reactions demonstrate that the method of soft harmonic constraints is significantly more efficient than fixed-atom optimization using Cartesian coordinates. While alternative optimization methods exist, which can constrain the anchor atoms without the need to use Cartesian coordinates, the harmonic-confiner approach has the advantage of being incredibly simple to implement in any electronic structure code. Geometry optimization with soft harmonic constraints results in displacement of the anchor atoms by no more than 0.04 Å (and often much less) for any of the examples considered here while preserving correct physics for the ZPE contributions. Proper local minima (with no imaginary frequencies) are obtained without any special steps taken to guarantee this. In contrast, the fixed-atom approach requires that the masses of the anchor atoms be set to infinity, which effectively excludes them from the normal modes and often introduces small imaginary frequencies in what are supposed to be local minima. The appearance of imaginary frequencies renders the fixed-atom approach useless for finite-temperature free energy calculations (e.g., barrier heights $\Delta G^{\ddagger}$), because low-frequency imaginary vibrations make sizable and unphysical contributions to the vibrational entropy. More generally, the fixed-atom approach introduces artifacts into the low-frequency part of the vibrational spectrum (see Figure S5) and should not be considered reliable for vibrational frequency calculations.

The use of soft harmonic constraints avoids artificial rigidity and strain in the truncated active-site models. In the specific case of the tautomerization of an α-keto acid by the enzyme 4-oxalocrotonate tautomerase, we are able to use harmonic constraints in conjunction with a smaller, 77-atom model

https://dx.doi.org/10.1021/acs.jpcb.9b11060
J. Phys. Chem. B 2020, 124, 1137−1147

system[28] to mimic the energetics of a larger 177-atom model. When fixed-atom constraints are used instead, these two models exhibit very different energy profiles.

Given the favorable results presented here and the abject simplicity of the harmonic-confiner approach, we see no reason why this method should not be quickly adopted in other quantum chemistry programs, as a replacement for fixed-atom optimizations. Use of soft harmonic confining potentials should quickly become the standard approach in "QM cluster" active-site models of enzyme-catalyzed reactions. This should be beneficial not only for QM cluster modeling, as currently construed, but also as the field shifts into even larger QM models using a combination of hardware and software improvements,[87,88] protein network analysis,[89] and fragment-based approximations.[90]

■ ASSOCIATED CONTENT

Supporting Information

The Supporting Information is available free of charge at https://pubs.acs.org/doi/10.1021/acs.jpcb.9b11060.

Additional numerical tests of the harmonic-confiner method (PDF)

Coordinates for all of the optimized stationary-point structures (TXT)

■ AUTHOR INFORMATION

Corresponding Author

John M. Herbert − *Department of Chemistry and Biochemistry, The Ohio State University, Columbus, Ohio 43210, United States;* orcid.org/0000-0002-1663-2278; Email: herbert@chemistry.ohio-state.edu

Author

Saswata Dasgupta − *Department of Chemistry and Biochemistry, The Ohio State University, Columbus, Ohio 43210, United States;* orcid.org/0000-0002-8014-8376

Complete contact information is available at: https://pubs.acs.org/10.1021/acs.jpcb.9b11060

Notes

The authors declare the following competing financial interest(s): J.M.H. serves on the Board of Directors of Q-Chem Inc.

■ ACKNOWLEDGMENTS

This work was supported by National Science Foundation Grant No. CHE-1665322. Calculations were performed at the Ohio Supercomputer Center under Project No. PAA0003.[91]

■ REFERENCES

(1) Senn, H. M.; Thiel, W. QM/MM methods for biological systems. *Top. Curr. Chem.* **2007**, *268*, 173−290.

(2) Senn, H. M.; Thiel, W. QM/MM methods for biomolecular systems. *Angew. Chem., Int. Ed.* **2009**, *48*, 1198−1229.

(3) Brunk, E.; Rothlisberger, U. Mixed quantum mechanical/molecular mechanical molecular dynamics simulations of biological systems in ground and electronically excited states. *Chem. Rev.* **2015**, *115*, 6217−6263.

(4) Friesner, R. A.; Guallar, V. Ab initio quantum chemical and mixed quantum mechanics/molecular mechanics (QM/MM) methods for studying enzymatic catalysis. *Annu. Rev. Phys. Chem.* **2005**, *56*, 389−427.

(5) Siegbahn, P. E. M.; Himo, F. Recent developments of the quantum chemical cluster approach for modeling enzyme reactions. *JBIC, J. Biol. Inorg. Chem.* **2009**, *14*, 643−651.

(6) Siegbahn, P. E. M.; Himo, F. The quantum chemical cluster approach for modeling enzyme reactions. *WIREs Comput. Mol. Sci.* **2011**, *1*, 323−336.

(7) Blomberg, M. R. A.; Borowski, T.; Himo, F.; Liao, R.-Z.; Siegbahn, P. E. M. Quantum chemical studies of mechanisms for metalloenzymes. *Chem. Rev.* **2014**, *114*, 3601−3658.

(8) Blomberg, M. R. A. How quantum chemistry can solve fundamental problems in bioenergetics. *Int. J. Quantum Chem.* **2015**, *115*, 1197−1201.

(9) Himo, F. Recent trends in quantum chemical modeling of enzymatic reactions. *J. Am. Chem. Soc.* **2017**, *139*, 6780−6786.

(10) Hopmann, K. H.; Himo, F. Quantum chemical modeling of the dehalogenation reaction of haloalcohol dehalogenase. *J. Chem. Theory Comput.* **2008**, *4*, 1129−1137.

(11) Georgieva, P.; Himo, F. Quantum chemical modeling of enzymatic reactions: The case of histone lysine methyltransferase. *J. Comput. Chem.* **2010**, *31*, 1707−1714.

(12) Hu, L.; Eliasson, J.; Heimdal, J.; Ryde, U. Do quantum mechanical energies calculated for small models of protein-active sites converge? *J. Phys. Chem. A* **2009**, *113*, 11793−11800.

(13) Hu, L.; Söderhjelm, P.; Ryde, U. On the convergence of QM/MM energies. *J. Chem. Theory Comput.* **2011**, *7*, 761−777.

(14) Sumner, S.; Söderhjelm, P.; Ryde, U. Effect of geometry optimizations on QM-cluster and QM/MM studies of reaction energies in proteins. *J. Chem. Theory Comput.* **2013**, *9*, 4205−4214.

(15) Liao, R.-Z.; Thiel, W. Comparison of QM-only and QM/MM models for the mechanism of tungsten-dependent acetylene hydratase. *J. Chem. Theory Comput.* **2012**, *8*, 3793−3803.

(16) Liao, R.-Z.; Thiel, W. Convergence in the QM-only and QM/MM modeling of enzymatic reactions: A case study for acetylene hydratase. *J. Comput. Chem.* **2013**, *34*, 2389−2397.

(17) Kulik, H. J.; Zhang, J.; Klinman, J. P.; Martnez, T. J. How large should the QM region be in QM/MM calculations? The case of catechol -methyltransferase. *J. Phys. Chem. B* **2016**, *120*, 11381−11394.

(18) Karelina, M.; Kulik, H. J. Systematic quantum mechanical region determination in QM/MM simulation. *J. Chem. Theory Comput.* **2017**, *13*, 563−576.

(19) Kulik, H. J. Large-scale QM/MM free energy simulations of enzyme catalysis reveal the influence of charge transfer. *Phys. Chem. Chem. Phys.* **2018**, *20*, 20650−20660.

(20) Yang, Z.; Mehmood, R.; Wang, M.; Qi, H. W.; Steeves, A. H.; Kulik, H. J. Revealing quantum mechanical effects in enzyme catalysis with large-scale electronic structure simulation. *React. Chem. Eng.* **2019**, *4*, 298−315.

(21) Scheraga, H. A. Influence of interatomic interactions on the structure and stability of polypeptides and proteins. *Biopolymers* **1981**, *20*, 1877−1899.

(22) Scheraga, H. A. Recent progress in the theoretical treatment of protein folding. *Biopolymers* **1983**, *22*, 1−14.

(23) Shao, Y.; et al. Advances in molecular quantum chemistry contained in the Q-Chem 4 program package. *Mol. Phys.* **2015**, *113*, 184−215.

(24) Valiev, M.; Bylaska, E. J.; Govind, N.; Kowalski, K.; Straatsma, T. P.; van Dam, H. J. J.; Wang, D.; Nieplocha, J.; Apra, E.; Windus, T. L.; de Jong, W. A. NWChem: A comprehensive and scalable open-source solution for large scale molecular simulations. *Comput. Phys. Commun.* **2010**, *181*, 1477−1489.

(25) te Velde, G.; Bickelhaupt, F. M.; Baerends, E. J.; Guerra, C. F.; van Gisbergen, S. J. A.; Snijders, J. G.; Ziegler, T. Chemistry with ADF. *J. Comput. Chem.* **2001**, *22*, 931−967.

(26) Schlegel, H. B. Geometry optimization. *WIREs Comput. Mol. Sci.* **2011**, *1*, 790−809.

(27) Jin, S.; Head, J. D. Theoretical investigation of molecular water adsorption on the Al(111) surface. *Surf. Sci.* **1994**, *318*, 204−216.

(28) Sevastik, R.; Himo, F. Quantum chemical modeling on enzymatic reactions: The case of 4-oxalocrotonate tautomerase. *Bioorg. Chem.* **2007**, *35*, 444−457.
(29) Georgieva, P.; Himo, F. Density functional theory study of the reaction mechanism of the DNA repairing enzyme alkylguanine alkyltransferase. *Chem. Phys. Lett.* **2008**, *463*, 214−218.
(30) Liao, R.-Z.; Yu, J.-G.; Raushel, F. M.; Himo, F. Theoretical investigation of the reaction mechanism of the dinuclear zinc enzyme dihydroorotase. *Chem. - Eur. J.* **2008**, *14*, 4287−4292.
(31) Chen, S.-L.; Marino, T.; Fang, W.-H.; Russo, N.; Himo, F. Peptide hydrolysis by the binuclear zinc enzyme aminopeptidase from *Aeromonas proteolytica*: A density functional theory study. *J. Phys. Chem. B* **2008**, *112*, 2494−2500.
(32) Chen, S.-L.; Fang, W.-H.; Himo, F. Reaction mechanism of the binuclear zinc enzyme glyoxalase II—A theoretical study. *J. Inorg. Biochem.* **2009**, *103*, 274−281.
(33) Georgieva, P.; Wu, Q.; McLeish, M. J.; Himo, F. The reaction mechanism of phenylethanolamine -methyltransferase: A density functional theory study. *Biochim. Biophys. Acta, Proteins Proteomics* **2009**, *1794*, 1831−1837.
(34) Yang, L.; Liao, R.-Z.; Yu, J.-G.; Liu, R.-Z. DFT study on the mechanism of *Escherichia coli* inorganic pyrophosphatase. *J. Phys. Chem. B* **2009**, *113*, 6505−6510.
(35) Liao, R.-Z.; Yu, J.-G.; Himo, F. Reaction mechanism of the trinuclear zine enzyme phospholipase C: A density functional theory study. *J. Phys. Chem. B* **2010**, *114*, 2533−2540.
(36) Lou, M.; Burger, S. K.; Gilpin, M. E.; Gawuga, V.; Capretta, A.; Berti, P. J. Transition state analysis of enolpyruvylshikimate 3-phosphate (EPSP) synthase (AroA)-catalyzed EPSP hydrolysis. *J. Am. Chem. Soc.* **2012**, *134*, 12958−12969.
(37) Lind, M. E. S.; Himo, F. Theoretical study of reaction mechanism and stereoselectivity of arylmalonate decarboxylase. *ACS Catal.* **2014**, *4*, 4153−4160.
(38) Svensson, F.; Engen, K.; Lundbäck, T.; Larhed, M.; Sköld, C. Virtual screening for transition state analogue inhibitors of IRAP based on quantum mechanically derived reaction coordinates. *J. Chem. Inf. Model.* **2015**, *55*, 1984−1993.
(39) Cassimjee, K. E.; Manta, B.; Himo, F. A quantum chemical study of the -transaminase reaction mechanism. *Org. Biomol. Chem.* **2015**, *13*, 8453−8464.
(40) Sheng, X.; Lind, M. E. S.; Himo, F. Theoretical study of the reaction mechanism of phenolic acid decarboxylase. *FEBS J.* **2015**, *282*, 4703−4713.
(41) Planas, F.; Sheng, X.; McLeish, M. J.; Himo, F. A theoretical study of the benzoylformate decarboxylase reaction mechanism. *Front. Chem.* **2018**, *6*, 205.
(42) Wei, W.-J.; Qian, H.-X.; Wang, W.-J.; Liao, R.-Z. Computational understanding of the selectivities in metalloenzymes. *Front. Chem.* **2018**, *6* (638), 1−22.
(43) Jensen, J. H. Predicting accurate absolute binding energies in aqueous solution: Thermodynamic considerations for electronic structure methods. *Phys. Chem. Chem. Phys.* **2015**, *17*, 12441−12451.
(44) Bootsma, A. N.; Wheeler, S. E. Popular integration grids can result in large errors in DFT-computed free energies. 2019. ChemRxiv. DOI: 10.26434/chemrxiv.8864204.v5.
(45) Senn, H. M.; Thiel, S.; Thiel, W. Enzymatic hydroxylation in -hydroxybenzoate hydroxylase: A case study for QM/MM molecular dynamics. *J. Chem. Theory Comput.* **2005**, *1*, 494−505.
(46) Hu, P.; Zhang, Y. Catalytic mechanism and product specificity of the histone lysine methyltransferase SET7/9: An ab initio QM/MM-FE study with multiple initial structures. *J. Am. Chem. Soc.* **2006**, *128*, 1272−1278.
(47) Senn, H. M.; Kästner, J.; Breidung, J.; Thiel, W. Finite-temperature effects in enzymatic reactions—insights from QM/MM free-energy simulations. *Can. J. Chem.* **2009**, *87*, 1322−1337.
(48) Lonsdale, R.; Hoyle, S.; Grey, D. T.; Ridder, L.; Mulholland, A. J. Determinants of reactivity and selectivity in soluble epoxide hydrolase from quantum mechanics molecular mechanics modeling. *Biochemistry* **2012**, *51*, 1774−1786.
(49) Kazemi, M.; Himo, F.; Åqvist, J. Enzyme catalysis by entropy without Circe effect. *Proc. Natl. Acad. Sci. U. S. A.* **2016**, *113*, 2406−2411.
(50) Mulholland, A. J. Dispelling the effects of a sorceress in enzyme catalysis. *Proc. Natl. Acad. Sci. U. S. A.* **2016**, *113*, 2328−2330.
(51) Blomberg, M. R. A.; Siegbahn, P. E. M. Mechanism for NO generation in bacterial nitric oxide reductase: A quantum chemical study. *Biochemistry* **2012**, *51*, 5173−5186.
(52) Sheng, X.; Zhu, W.; Huddleston, J.; Xiang, D. F.; Raushel, F. M.; Richards, N. G. J.; Himo, F. A combined experimental-theoretical study of the LigW-catalyzed decarboxylation of 5-carboxyvanillate in the metabolic pathway for lignin degradation. *ACS Catal.* **2017**, *7*, 4968−4974.
(53) Baker, J.; Kessi, A.; Delley, B. The generation and use of delocalized internal coordinates in geometry optimization. *J. Chem. Phys.* **1996**, *105*, 192−212.
(54) Cremer, D.; Wu, A.; Larsson, A.; Kraka, E. Some thoughts about bond enegies, bond lengths, and force constants. *J. Mol. Model.* **2000**, *6*, 396−412.
(55) Miyamoto, K.; Ohta, H. Enzyme-mediated asymmetric decarboxylation of disubstituted malonic acids. *J. Am. Chem. Soc.* **1990**, *112*, 4077−4078.
(56) Miyamoto, K.; Ohta, H. Asymmetric decarboxylation of disubstituted malonic acid by *Alcaligenes bronchisepticus* KU 1201. *Biocatalysis* **1991**, *5*, 49−60.
(57) Miyamoto, K.; Ohta, H. Purification and properties of a nove arylmalonate decarboxylase from *Alcaligenes bronchisepticus* (KU) 1201. *Eur. J. Biochem.* **1992**, *210*, 475−481.
(58) Reetz, M. T. Laboratory evolution of stereoselective enzymes: A prolific source of catalysts for asymmetric reactions. *Angew. Chem., Int. Ed.* **2011**, *50*, 138−174.
(59) Kourist, R.; Guterl, J.-K.; Miyamoto, K.; Sieber, V. Enzymatic decarboxylation—an emerging reaction for chemicals production from renewable resources. *ChemCatChem* **2014**, *6*, 689−701.
(60) Matoishi, K.; Ueda, M.; Miyamoto, K.; Ohta, H. Mechanism of asymmetric debarboxylation of α-aryl-α-methylmalonate catalyzed by arylmalonate decarboylase originated from *Alcaligenes bronchisepticus*. *J. Mol. Catal. B: Enzym.* **2004**, *27*, 161−168.
(61) Okrasa, K.; Levy, C.; Wilding, M.; Goodall, M.; Baudendistel, N.; Hauer, B.; Leys, D.; Micklefield, J. Structure-guided directed evolution of alkenyl and arylmalonate decarboxylases. *Angew. Chem., Int. Ed.* **2009**, *48*, 7691−7694.
(62) Okrasa, K.; Levy, C.; Hauer, B.; Baudendistel, N.; Leys, D.; Micklefield, J. Structure and mechanism of an unusual malonate decarboxylase and related racemases. *Chem. - Eur. J.* **2008**, *14*, 6609−6613.
(63) Miyazaki, M.; Kakidani, H.; Hanzawa, S.; Ohta, H. Cysteine 188 revealed as being critical for the enzyme activity of arylmalonate decarboxylase by site-directed mutagenesis. *Bull. Chem. Soc. Jpn.* **1997**, *70*, 2765−2769.
(64) Terao, Y.; Miyamoto, K.; Ohta, H. Introduction of a single mutation changes arylmalonate decarboxylase to racemase. *Chem. Commun.* **2006**, 3600−3602.
(65) Kourist, R.; Miyauchi, Y.; Uemura, D.; Miyamoto, K. Engineering the promiscuous racemase activity of an arylmalonate decarboxylase. *Chem. - Eur. J.* **2011**, *17*, 557−563.
(66) Miyauchi, Y.; Kourist, R.; Uemura, D.; Miyamoto, K. Dramatically improved catalytic activity of an artificial (*S*)-selective arylmalonate decarboxylase by structure-guided directed evolution. *Chem. Commun.* **2011**, *47*, 7503−7505.
(67) Grimme, S.; Antony, J.; Ehrlich, S.; Krieg, H. A consistent and accurate *ab initio* parameterization of density functional dispersion correction (DFT-D) for the 94 elements H−Pu. *J. Chem. Phys.* **2010**, *132*, 154104.
(68) Grimme, S.; Ehrlich, S.; Goerigk, L. Effect of the damping function in dispersion corrected density functional theory. *J. Comput. Chem.* **2011**, *32*, 1456−1465.
(69) Gill, P. M. W.; Johnson, B. G.; Pople, J. A. A standard grid for density-functional calculations. *Chem. Phys. Lett.* **1993**, *209*, 506−512.

(70) Herbert, J. M.; Lange, A. W. Polarizable continuum models for (bio)molecular electrostatics: Basic theory and recent developments for macromolecules and simulations. In *Many-Body Effects and Electrostatics in Biomolecules*; Cui, Q., Ren, P., Meuwly, M., Eds.; Pan Stanford: 2016; Chapter 11, pp 363−416.
(71) Lange, A. W.; Herbert, J. M. Polarizable continuum reaction-field solvation models affording smooth potential energy surfaces. *J. Phys. Chem. Lett.* **2010**, *1*, 556−561.
(72) Lange, A. W.; Herbert, J. M. A smooth, nonsingular, and faithful discretization scheme for polarizable continuum models: The switching Gaussian approach. *J. Chem. Phys.* **2010**, *133*, 244111.
(73) Miyamoto, K.; Ohta, H.; Osamura, Y. Effect of conformation of the substrate on enzymatic eecarboxylation of α-arylmalonic acid. *Bioorg. Med. Chem.* **1994**, *2*, 469−475.
(74) Chen, L. H.; Kenyon, G. L.; Curtin, F.; Harayama, S.; Bembenek, M. E.; Hajipour, G.; Whitman, C. P. 4-Oxalocrotonate tautomerase, an enzyme composed of 62 amino acid residues per monomer. *J. Biol. Chem.* **1992**, *267*, 17716−17721.
(75) Subramanya, H. S.; Roper, D. I.; Dauter, Z.; Dodson, E. J.; Davies, G. J.; Wilson, K. S.; Wigley, D. B. Enzymatic ketonization of 2-hydroxymuconate: Specificity and mechanism investigated by the crystal structures of two isomerases. *Biochemistry* **1996**, *35*, 792−802.
(76) Taylor, A. B.; Czerwinski, R. M.; Johnson, W. H.; Whitman, C. P.; Hackert, M. L. Crystal structure of 4-oxalocrotonate tautomerase inactivated by 2-oxo-3-pentynoate at 2.4 Å resolution: Analysis and implications for the mechanism of inactivation and catalysis. *Biochemistry* **1998**, *37*, 14692−14700.
(77) Cisneros, G. A.; Liu, H.; Zhang, Y.; Yang, W. Ab initio QM/MM study shows there is no general acid in the reaction catalyzed by 4-oxalocrotonate tautomerase. *J. Am. Chem. Soc.* **2003**, *125*, 10384−10393.
(78) Cisneros, G. A.; Wang, M.; Silinski, P.; Fitzgerald, M. C.; Yang, W. The protein backbone makes important contributions to 4-oxalocrotonate tautomerase enzyme catalysis: Understanding from theory and experiment. *Biochemistry* **2004**, *43*, 6885−6892.
(79) Cisneros, G. A.; Wang, M.; Silinski, P.; Fitzgerald, M. C.; Yang, W. Theoretical and experimental determination on two substrates turned over by 4-oxalocrotonate tautomerase. *J. Phys. Chem. A* **2006**, *110*, 700−708.
(80) Fitzgerald, M. C.; Chernushevich, I.; Standing, K. G.; Whitman, C. P.; Kent, S. B. Probing the oligomeric structure of an enzyme by electrospray ionization time-of-flight mass spectrometry. *Proc. Natl. Acad. Sci. U. S. A.* **1996**, *93*, 6851−6856.
(81) Stivers, J. T.; Abeygunawardana, C.; Mildvan, A. S.; Hajipour, G.; Whitman, C. P.; Chen, L. H. Catalytic role of the amino-terminal proline in 4-oxalocrotonate tautomerase: Affinity labeling and heteronuclear NMR studies. *Biochemistry* **1996**, *35*, 803−813.
(82) Czerwinski, R. M.; Harris, T. K.; Massiah, M. A.; Mildvan, A. S.; Whitman, C. P. The structural basis for the perturbed p of the catalytic base in 4-oxalocrotonate tautomerase: Kinetic and structural effects of mutations of Phe-50. *Biochemistry* **2001**, *40*, 1984−1995.
(83) Harris, T. K.; Czerwinski, R. M.; Johnson, W. H.; Legler, P.; Abeygunawardana, C.; Massiah, M. A.; Stivers, J. T.; Whitman, C. P.; Mildvan, A. S. Kinetic, stereochemical, and structural effects of mutations of the active site arginine residues in 4-oxalocrotonate tautomerase. *Biochemistry* **1999**, *38*, 12343−12357.
(84) Whitman, C. P. The 4-oxalocrotonate tautomerase family of enzymes: How nature makes new enzymes using a β−α−β structural motif. *Arch. Biochem. Biophys.* **2002**, *402*, 1−13.
(85) Metanis, N.; Brik, A.; Dawson, P. E.; Keinan, E. Electrostatic interactions dominate the catalytic contribution of Arg39 in 4-oxalocrotonate tautomerase. *J. Am. Chem. Soc.* **2004**, *126*, 12726−12727.
(86) Tuttle, T.; Thiel, W. Substrate orientation in 4-oxalocrotonate tautomerase and its effect on QM/MM energy profiles. *J. Phys. Chem. B* **2007**, *111*, 7665−7674.
(87) Kulik, H. J.; Luehr, N.; Ufimtsev, I. S.; Martinez, T. J. Ab initio quantum chemistry for protein structures. *J. Phys. Chem. B* **2012**, *116*, 12501−12509.
(88) Tornai, G. J.; Ladjánszki, I.; Rák, A.; Kis, G.; Cserey, G. Calculation of quantum chemical two-electron integrals by applying compiler technology on GPU. *J. Chem. Theory Comput.* **2019**, *15*, 5319−5331.
(89) Summers, T. J.; Daniel, B. P.; Cheng, Q.; DeYonker, N. J. Quantifying inter-residue contact through interaction energies. *J. Chem. Inf. Model.* **2019**, *59*, 5034−5044.
(90) Herbert, J. M. Fantasy versus reality in fragment-based quantum chemistry. *J. Chem. Phys.* **2019**, *151*, 170901.
(91) "Ohio Supercomputer Center", http://osc.edu/ark:/19495/f5s1ph73.

https://dx.doi.org/10.1021/acs.jpcb.9b11060
J. Phys. Chem. B 2020, 124, 1137−1147